Heliyon 9 (2023) e20006

Contents lists available at ScienceDirect

Heliyon

journal homepage: www.cell.com/heliyon

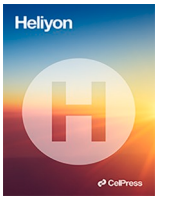

Valence state switching and reversible emission tunability of A_2SiO_4 (A = Ba, Sr, and Ca) with two-site substitution of Eu ions through simple thermal treatment

M.J. Jeong, S.W. Lee, S.W. Wi, K.C. Lee, Y.S. Lee *

Department of Physics and Integrative Institute of Basic Sciences, Soongsil University, Seoul, 06978, Republic of Korea

ARTICLE INFO

Keywords:
A_2SiO_4
Eu^{2+}/Eu^{3+}
Photoluminescence
Valence state switching
Thermal treatment
Two-site occupation

ABSTRACT

We investigated the changes in the structural and luminescent properties of Eu-ion-doped A_2SiO_4 (A_2SiO_4:Eu, A = Ba, Sr, and Ca) by annealing in oxidizing and reducing atmospheres. The initially synthesized samples displayed distinct, intense red emissions at approximately 600 and 700 nm, which can be attributed to the presence of Eu^{3+} ions. The emission intensity of Eu^{3+} was the strongest in Ca_2SiO_4:Eu, which exhibited the lowest lattice symmetry among the three samples. Remarkably, following annealing in a reducing atmosphere (H_2), the previously observed red emission vanished, and instead, a strong green emission at around 500 nm, which is characteristic of Eu^{2+} ions. Because of the two occupation sites of the Eu ions in A_2SiO_4, the emission of Eu^{2+} strongly depends on the excitation wavelength, which is the most evident in Ca_2SiO_4:Eu. Conversely, after annealing in an oxidizing atmosphere (O_2), the emission in the green region was suppressed and the emission in the red region returned. The reversible transition between two oxidation states occurred repeatedly by alternating H_2 and O_2 annealing, resulting in good color tunability in wide visible region with a simple ambient annealing process in a single compound.

1. Introduction

Rare earth (RE) ion-doped oxides, that is, phosphors, have attracted considerable attention for several photoelectronic applications such as three-dimensional displays, solid-state lighting, bio-imaging, and photocatalysis [1–3]. The colors of the phosphors are determined mainly by the RE ions, whose 4f-4f and 4f-5d transitions are the origin of the luminescent properties. Each RE ion has its own 4f orbital energy levels, which are rather insensitive to the host material owing to the screening effect of the 5s and 5p orbitals. Because the color of the phosphor depends strongly on the RE elements, color tunability of the phosphor is an important issue. Changes in the host material, doping concentration, multiple doping, site occupancy engineering, and charge transfer between RE ions can be employed to improve the color tunability of phosphors [4].

Eu ions have good color tunability according to their valence state [5]. Eu ions can be stably present as Eu^{2+} or Eu^{3+}. The luminescence of trivalent Eu^{3+} ions is caused by $4f^6 \rightarrow 4f^6$ transitions, resulting in narrow and weak emission spectra. Under ultraviolet and violet-blue excitation, Eu^{3+} ions show emissions in a range of 570–710 nm because of the $^5D_0 \rightarrow {}^7F_J$ (J = 0, 1, 2, 3, and 4) transitions. In contrast, the divalent Eu^{2+} ion shows a broad and strong emission spectrum owing to the allowed $4f^65d^1 \rightarrow 4f^7$ transition. The energy levels of the 5d orbitals in Eu^{2+} ions are significantly influenced by the crystal field. As a result, the absorption and emission bands of

* Corresponding author.
E-mail address: ylee@ssu.ac.kr (Y.S. Lee).

https://doi.org/10.1016/j.heliyon.2023.e20006
Received 24 August 2023; Received in revised form 6 September 2023; Accepted 8 September 2023
Available online 9 September 2023

Eu^{2+} ions exhibit considerable variation, depending on the specific host crystal material. These bands can span a wide range of wavelengths, extending from the ultraviolet (UV) to the blue region of the electromagnetic spectrum [6,7]. Thanks to the above-mentioned sharp contrast between two luminescent behaviors, we could have good tunability of the luminescence in oxide phosphors doped with the Eu ions under control of their valence states, e.g., 2+/3+, which could lead to high optoelectronic application potential [8]. However, few studies have demonstrated the broad color tunability of the european ions according to their valence states of a single material.

A_2SiO_4 (A = Ba, Sr, and Ca) compounds have proven to be suitable hosts for luminescent lanthanide ions with several advantages, such as good chemical and thermal stability, abundant crystal structure, and relatively easy synthesis, including low sintering temperatures and inexpensive raw materials [9–11]. Therefore, they have been considered for applications in phosphors and scintillators. In addition, the crystalline structures of A_2SiO_4 change considerably with the A ion. The structure of Ba_2SiO_4 is orthorhombic and its space group is *Pnma* [12]. Sr_2SiO_4 has two stable structural phases, α′ and β. α′-Sr_2SiO_4 has an orthorhombic structure with the space group *Pnma*, whereas β-Sr_2SiO_4 has a monoclinic structure with the space group $P2_1/c$ [13–15]. Ca_2SiO_4 has two phases, γ- and β-phases are stable at room temperature. The γ-phase has an orthorhombic structure (space group *Pnma*), whereas the β-phase has a monoclinic structure with the space group $P2_1/c$. In addition, A_2SiO_4 (A = Ba, Sr, and Ca) compounds have two cation sites where Eu ions can be doped. Two cation sites in A_2SiO_4 result in different Eu^{2+} emissions depending on site occupancy. Moreover, because the ionic radii of two cation sites are similar to those of Eu^{2+} and Eu^{3+} ions, Eu ions can exist in both divalent and trivalent states in A_2SiO_4 [16]. Therefore, this series of compounds can be a good platform for investigating the relationship between structural and luminescent properties for Eu ion emission.

There have been several studies focusing on the luminescent properties of high efficiency emitting [17,18], and systematic peak shift [19] of the Eu ion in A_2SiO_4, no studies have been conducted on the switching through thermal treatment between the divalent and trivalent states and the related changes in the structural and luminescent properties of Eu ion-doped A_2SiO_4. In this study, A_2SiO_4 (A = Ba, Sr, or Ca) doped with Eu ions was synthesized using a solid-state reaction method. The structural and luminescent characteristics of the phosphors were studied by changing the valence state of the Eu ions through annealing in oxidizing and reducing atmospheres. The emission properties of Eu^{2+} and Eu^{3+} vary significantly depending on the ions at A-site, which are relevant to the lattice distortion in the compounds. We confirmed that the Eu-ion-doped A_2SiO_4 showed good color tunability with a simple ambient annealing process.

2. Experimental

We synthesized Eu-ion-doped A_2SiO_4 (A_2SiO_4:Eu) compounds, where A = Ba, Sr, or Ca, through a solid-state reaction method. The synthesis process involved blending high-purity raw materials: SiO_2 (99.9%), Eu_2O_3 (99.99%), $BaCO_3$ (99.98%), $SrCO_3$ (99.9%), and $CaCO_3$ (99.95%) in a specific ratio of SiO_2: Eu_2O_3: (Ba/Sr/Ca)CO_3 = 1:0.01:1.98, enabling the substitution of Eu ions for A ions. The doping concentration of Eu^{3+} was set at 0.02. The resulting mixture was calcined at 1100 °C for 2 h and then formed into pellets. Subsequently, the pellet samples were sintered at 1250 °C for 4 h in an ambient air atmosphere. For an investigation into the environmental dependence of the materials, we subjected the sintered samples to the 900 °C annealing processes (4 h) in two different atmospheres: O_2 and H_2 (H_2:Ar = 0.04:0.96).

We performed X-ray diffraction (XRD) patterns in examine the structural characteristics of our samples. We measured luminescent spectra using a JASCO FP-8500 spectrofluorometer, which utilized a Xe lamp as the excitation source. Time-resolved photoluminescence (TRPL) spectra were obtained using a spectrofluorometer (FluoroMax Plus, HORIBA) equipped with a Xe arc lamp.

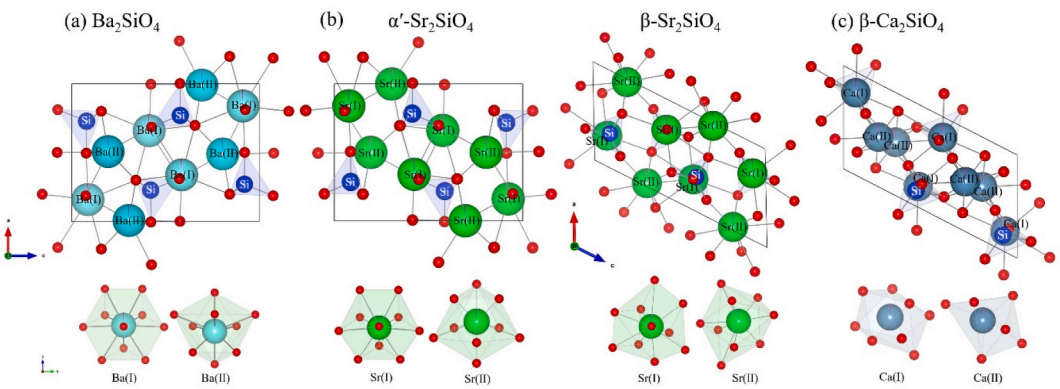

Fig. 1. The structure of (a) Ba_2SiO_4, (b) α'-Sr_2SiO_4, β-Sr_2SiO_4, and (c) β-Ca_2SiO_4. Two cation sites (A(I) and A(II)) are indicated under each structure.

3. Results and discussion

3.1. Structural properties of A_2SiO_4:Eu

First, we review the structural properties of A_2SiO_4 (A = Ba, Sr, and Ca), which strongly depend on the A ions. Fig. 1 shows the structure of A_2SiO_4. As explained in the Introduction section, The structure of Ba_2SiO_4 is orthorhombic and its space group is *Pnma* [12]. The Ba ion has two cation sites: Ba(I) in a 10-coordinate system and Ba(II) in a 9-coordinate system (Fig. 1(a)) [20]. Sr_2SiO_4 has two stable structural phases, α′ and β. α′-Sr_2SiO_4 has an orthorhombic structure with the space group *Pnma*, whereas β-Sr_2SiO_4 has a monoclinic structure with the space group $P2_1/c$ [13–15]. Both phases are stable at room temperature and coexist easily. The transition between the two phases is possible with a coordination structure rearrangement at a short distance [20–22]. Similar to Ba_2SiO_4, both phases of Sr_2SiO_4 have two cation sites: Sr(I) with 10 coordinates and Sr(II) in a 9-coordinate (Fig. 1(b)) [20,21,23,24]. Ca_2SiO_4 has five phases that are stable at high temperatures in the order of α, α'_L, α'_H, β, and γ. Among them, the γ- and β-phases are stable at room temperature, but in general, the γ-phase has higher thermal stability than the β-phase. According to a recent study, impurity ions could make the β-phase stabler, acting as a stabilizer [25–28]. The γ-phase has an orthorhombic structure (space group *Pnma*), whereas the β-phase has a monoclinic structure with the space group $P2_1/c$. In both phases, the Ca ion has two cation sites: Ca(I) and Ca(II) in the 6-coordinate space in the γ-phase and Ca(I) in the 8-coordinate space and Ca(II) in the 7-coordinate space in the β-phase (Fig. 1(c)) [25].

Fig. 2 shows the XRD patterns of A_2SiO_4:Eu before and after H_2/O_2 annealing. Our Ba_2SiO_4:Eu samples exhibited the same XRD patterns as undoped Ba_2SiO_4 (JCPDS 26–1403), and no change in the XRD patterns was observed upon H_2/O_2 annealing (Fig. 2(a)). The XRD pattern of the as-synthesized Sr_2SiO_4:Eu appeared to be a mixture of the two phase ratios of α′-Sr_2SiO_4 (JCPDS 39–1256) and β-Sr_2SiO_4 (JCPDS 38–2071) (Fig. 2(b)). The characteristic peaks for each phase were observed at $2\theta = 27.2^\circ$ for α′-Sr_2SiO_4 and $2\theta = 27.7^\circ$ and 32.4° for β-Sr_2SiO_4. Interestingly, the intensity of the peak at $2\theta = 27.2^\circ$ increased in the H_2 annealed samples and decreased in the O_2 annealed samples, whereas those at $2\theta = 27.7^\circ$ and 32.4° exhibited the opposite trend. This change implies that the H_2 annealing process increased the volume fraction of the α′-phase, as detailed by the Rietveld refinement analysis. In Ca_2SiO_4:Eu, the XRD pattern matched well with that of β-Ca_2SiO_4 (JCPDS 33–0302) before and after H_2/O_2 annealing (Fig. 2(c)). This indicates that doping with Eu ions makes the β-phase more stable than then γ-phase in Ca_2SiO_4 [25–28].

To quantitatively analyze the structural changes induced by H_2/O_2 annealing, we performed Rietveld refinement analysis of the XRD patterns of A_2SiO_4:Eu (Fig. 3(a–f)). Rietveld refinement analysis showed agreement between the XRD data and the theoretical data calculated using the relevant lattice constants and atomic positions [29]. The calculated data, measured data, and the difference between the two sets of data are represented by the red lines, empty circles, and blue lines, respectively. The weighted profile R-factors (R_{wp}) from the Rietveld refinement results were in the range of 7.78–21.05, and the goodness of fit (χ^2) values from the results were in the range of 1.13–3.71. These values indicate that the Rietveld refinement results were appropriate. Through Rietveld refinement analysis, we confirmed that the structure of Ba_2SiO_4:Eu was orthorhombic (*Pnma*), the structure of Sr_2SiO_4:Eu was a mixture of orthorhombic (α′, *Pnma*) and monoclinic (β, $P2_1/c$), and the structure of Ca_2SiO_4:Eu was monoclinic (β, $P2_1/c$) [6,18,30]. Interestingly, the weight ratios of the α′- and β-phases of Sr_2SiO_4:Eu were approximately 1:1 in the H_2 annealed sample, but the ratio changed to 1:2 in the O_2 annealed sample. This result suggests that the α′-phase prefers an oxygen-deficient environment. According to Catti et al. the bond valence sums (BVS) are lower in the α′-phase than in the β-phase: BVS = 1.58 in α′-phase and 1.78 in β-phase [15]. In the oxygen deficient environment (H_2 annealing), the Sr(I) atoms are no longer bonded with the oxygen atoms, which reduces the BVS and thus makes the α′-phase preferred [31]. We summaried the lattice constant of A_2SiO_4:Eu obtained through Rietveld refinement and the

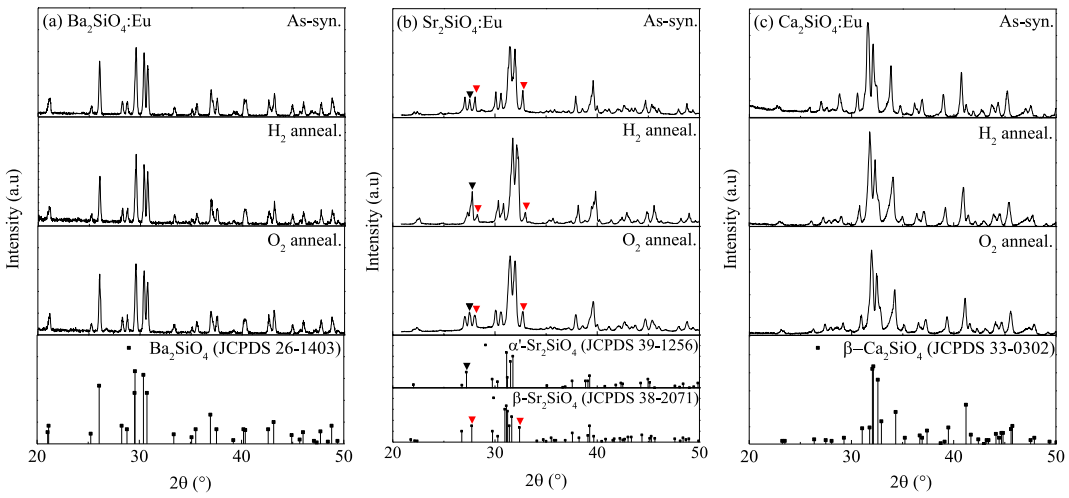

Fig. 2. The XRD patterns of (a) Ba_2SiO_4:Eu (JCPDS 26–1403), (b) Sr_2SiO_4:Eu (JCPDS 39–1256, 38–2071), and (c) Ca_2SiO_4:Eu (JCPDS 33–0302) before and after H_2/O_2 annealing. In (b), the triangles indicate the characteristic peaks of the α′- and β phases.

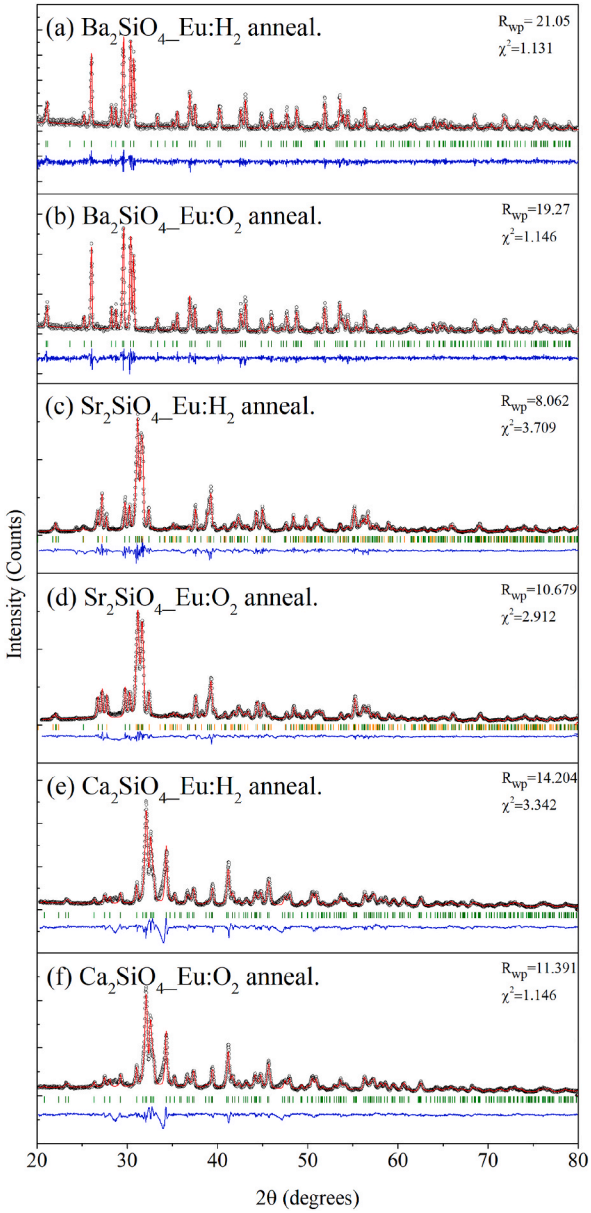

Fig. 3. The Rietveld refinement analysis data of (a) $Ba_2SiO_4:Eu^{2+}$ (b) $Ba_2SiO_4:Eu^{3+}$, (c) $Sr_2SiO_4:Eu^{2+}$ (d) $Sr_2SiO_4:Eu^{3+}$, (e) $Ca_2SiO_4:Eu^{2+}$, and (f) $Ca_2SiO_4:Eu^{3+}$. The open circles (○) represent the XRD data, and the solid line (red) is calculated ones. A difference (Obs.-Cal.) plot is shown beneath. Tick marks above the difference data indicate the Bragg position (orange tick mark is α′-Sr_2SiO_4).

weight ratio of the α′- and β-phases of Sr_2SiO_4:Eu in Table 1. Our results suggest that the symmetry of the lattice should be lower for A = Ba (orthorhombic), Sr (orthorhombic + monoclinic), and Ca (monoclinic).

3.2. *Luminescence of A_2SiO_4:Eu in H_2 and O_2 annealing: Eu^{2+} vs. Eu^{3+}*

Fig. 4 shows the photoluminescence (PL) of our samples before and after the H_2 and O_2 annealings. The excitation wavelength (λ_{ex}) was set to 395 nm, which is the photoexcitation wavelength for both Eu^{2+} (4f-5d transition) and Eu^{3+} ($^7F_0$-$^5L_6$ transition). The as-synthesized A_2SiO_4:Eu exhibited emission peaks at approximately 600 and 700 nm, corresponding to the $^5D_0 \rightarrow {}^7F_j$ (j = 0, 1, 2, 3, and 4) transitions of Eu^{3+} (Fig. 4(a)), whereas the emissions corresponding to the $^5D_0 \rightarrow {}^7F_4$ transition (703 nm) were the strongest. This observation clearly indicates that the Eu ions in the as-synthesized state were trivalent. Among the three species, Ca_2SiO_4:Eu exhibits the strongest emission, possibly because of its low lattice symmetry.

To investigate the ambient dependence of the emission properties of A_2SiO_4:Eu, we performed the post-annealing of the as-

Table 1
Results of Rietveld refinement analysis of A_2SiO_4:Eu (A = Ba, Sr, and Ca): lattice constants (a, b, and c), angle (β), and cell volume (V).

Sample	Anneal	Phase	Weight ratio (%)	a(Å)	b(Å)	c(Å)	β(°)	V(Å^3)	χ^2	R_{wp}(%)
Ba_2SiO_4:Eu	H_2	–	–	7.51	5.81	10.22	–	445.93	1.13	21.05
	O_2	–	–	7.51	5.81	10.22	–	445.93	1.15	19.27
Sr_2SiO_4:Eu	H_2	α′	50.64	7.07	5.67	9.74	–	390.45	3.71	10.68
		β	49.36	5.66	7.08	11.05	118.13	442.80		
	O_2	α′	33.35	7.07	5.66	9.73	–	389.36	2.91	7.78
		β	66.65	5.65	7.08	11.03	118.15	441.22		
Ca_2SiO_4:Eu	H_2	β		5.51	6.75	10.44	117.21	388.29	3.34	14.20
	O_2	β		5.51	6.76	10.44	117.21	388.86	1.15	11.39

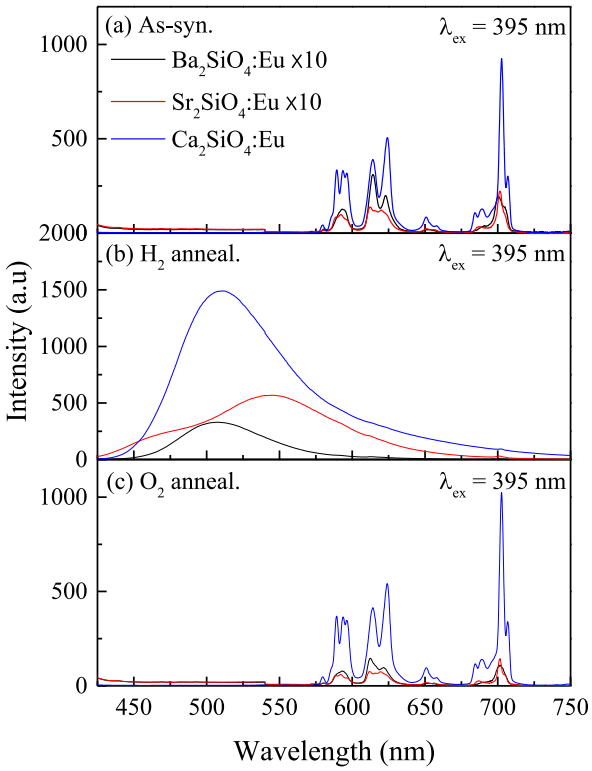

Fig. 4. (a) As-synthesized, (b) H_2 annealed, and (c) O_2 annealed PL spectra of A_2SiO_4:Eu (A = Ba, Sr, and Ca).

synthesized samples under an H_2 atmosphere. Interestingly, we observed strong and broad peaks at approximately 400–600 nm, which were assigned to the 5d-4f transition of Eu^{2+} (Fig. 4(b)). The PL intensity was the highest for Ca_2SiO_4:Eu^{2+}. The emergence of Eu^{2+} emission suggests that the Eu ions in A_2SiO_4:Eu can be easily converted from a trivalent state to a divalent state through the reduction process of annealing in H_2 atmosphere. We re-annealed the samples in an O_2 ambience, and their luinescnece re-exhibited a typical f-f emission in the range of 600–700 nm (Fig. 4(c)). This finding indicates that Eu^{2+} changed to Eu^{3+}, and that the annealing process in an O_2 environment can easily convert Eu ions from a divalent state to a trivalent state by oxidation.

To confirm the reversibility of the Eu ion valence state conversion, successive annealing in H_2 and O_2 atmospheres was repeated for

Table 2
Integration of PL intensities of A_2SiO_4:Eu at λ_{ex} = 330 nm (Eu^{2+}) and 395 nm (Eu^{3+}). The emission peak was calculated around 500 nm (Eu^{2+}) and 600–700 nm (Eu^{3+}).

Sample	As-synthesized	1st H_2 anneal	1st O_2 anneal	2nd H_2 anneal	2nd O_2 anneal
Ba_2SiO_4:Eu	773.8	94627.1	747.1	97489.4	741.2
Sr_2SiO_4:Eu	177.1	125935.2	172.8	109949.2	161.3
Ca_2SiO_4:Eu	20307.5	271654.7	19582.3	361257.3	18509.6

the A_2SiO_4:Eu samples. For the quantitative analysis of the change in PL intensity, we estimated the PL intensities of Eu^{2+} and Eu^{3+} by integrating the PL spectra in the spectral ranges of 450–550 nm and 580–720 nm, respectively (Table 2). The reversible behaviors in the integrated intensity of PL were clearly observed in A_2SiO_4:Eu for all three A ions under successive redox process (Fig. 5(a–c)). This result shows that the emission properties of A_2SiO_4:Eu could be easily manuplated by converting the Eu ion valence state through ambient treatment.

3.3. Luminescence properties of A_2SiO_4:Eu

3.3.1. Luminescent properties of $A_2SiO_4:Eu^{2+}$

To investigate the emission properties of Eu^{2+} in $A_2SiO_4:Eu^{2+}$ in depth, we recorded the emission spectra of the H_2 annealed samples at λ_{ex} = of 330 nm (Fig. 6(a–c)). We observed broad 5d-4f emission in Eu^{2+} near 500 nm [6,19,32–35]. Notably, Eu ions occupy two A-sites in A_2SiO_4, that is, the A(I) and A(II)sites. We denote the Eu ions substituted at the A(I) and A(II) sites as Eu(I) and Eu (II), respectively. The absorption and emission spectra of Eu^{2+} depend on the substitution sites because of different local lattice environments. We fitted the emission spectrum of A_2SiO_4:Eu with two bands, Peaks I and II, as shown in Fig. 6. We estimated the positions of Peak I to be 500 nm (2.48 eV), 490 nm (2.53 eV), and 510 nm (2.43 eV) and those of Peak II to be 535 nm (2.31 eV), 540 nm (2.30 eV), and 570 nm (2.18 eV); therefore, the difference in the two peak positions was 0.17 eV, 0.23 eV, and 0.25 eV for A = Ba, Sr, and Ca, respectively. The positions of the two emissions and their differences are associated with the crystal field strengths at the two cation sites doped with Eu ions in these materials. The details are discussed in Section 3.3.2.

The photoluminescence excitation (PLE) spectra were also measured by monitoring the emissions of Peaks I and II. As shown in Fig. 6, for the PLE spectra of Peak I (black line), all three A_2SiO_4:Eu samples exhibited a wide excitation band in the range of approximately 220–450 nm. The PLE spectra of Peak II (blue line) were measured and compared with those of Peak I. In $Ba_2SiO_4:Eu^{2+}$, the range of the PLE spectrum of Peak II was the same as that of Peak I, but weaker. The compounds $Sr_2SiO_4:Eu^{2+}$ and $Ca_2SiO_4:Eu^{2+}$ exhibited a weak peak II excitation intensity, but the excitation spectra spread up to 500 nm.

Interestingly, owing to the two substitution sites, the emission spectra depend strongly on the excitation wavelength. For a more detailed analysis, we measured the PL intensity of $A_2SiO_4:Eu^{2+}$ at different excitation wavelengths (Fig. 7). In Fig. 7(a), the PL intensity of $Ba_2SiO_4:Eu^{2+}$ hardly depended on the excitation wavelength because the excitation wavelength ranges of Peaks I and II were nearly identical. In $Sr_2SiO_4:Eu^{2+}$, as shown in Fig. 7(b), the PL intensity of Peak I was dominant near the short excitation wavelength, λ_{ex} = 310–360 nm, but with the photoexcitation of λ_{ex} increasing up to 400 nm, Peak I was suppressed, and then Peak II developed [19]. Similarly, the wavelength of the maximum PL intensity of $Ca_2SiO_4:Eu^{2+}$ changed significantly from 500 to 600 nm as the excitation

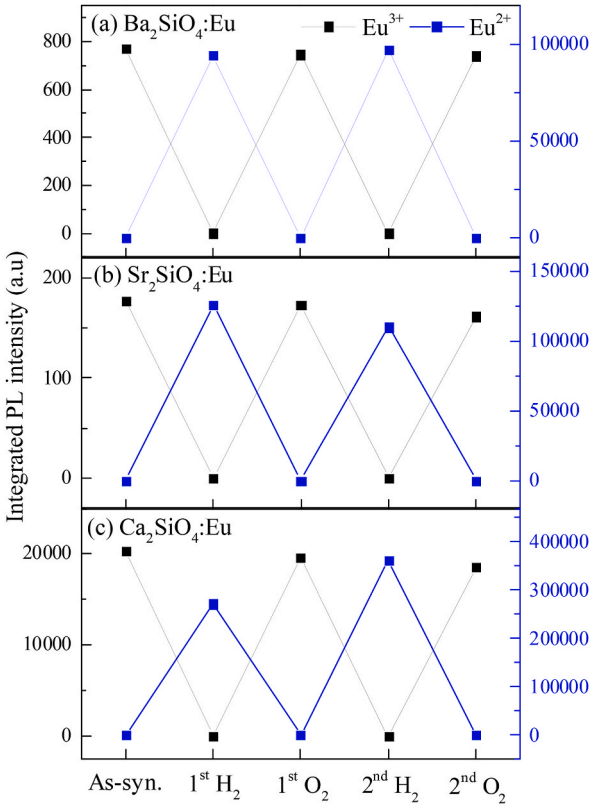

Fig. 5. Integrated PL intensities of the Eu^{2+}(blue squares) and Eu^{3+}(black squares) of (a) Ba_2SiO_4:Eu, (b) Sr_2SiO_4:Eu, and (c) Ca_2SiO_4:Eu.

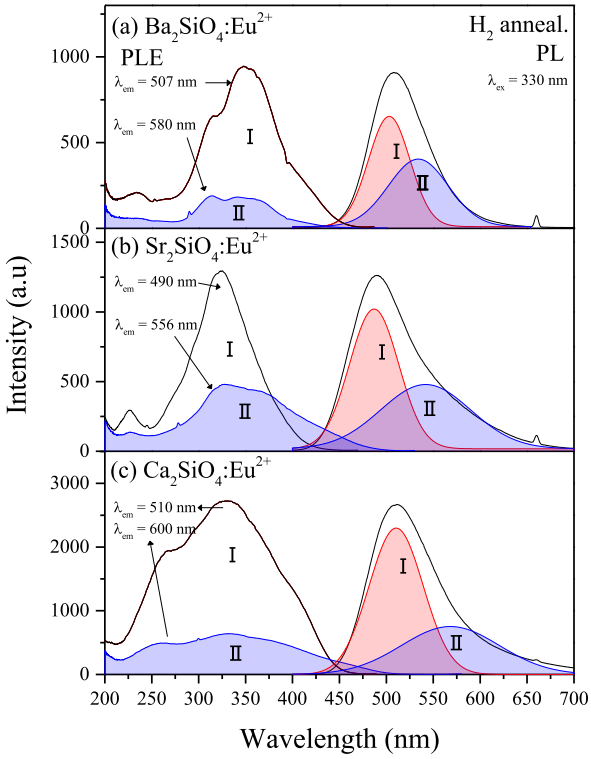

Fig. 6. The PL and PLE spectra of (a) $Ba_2SiO_4:Eu^{2+}$, (b) $Sr_2SiO_4:Eu^{2+}$, and (c) $Ca_2SiO_4:Eu^{2+}$ annealed in an H_2 atmosphere.

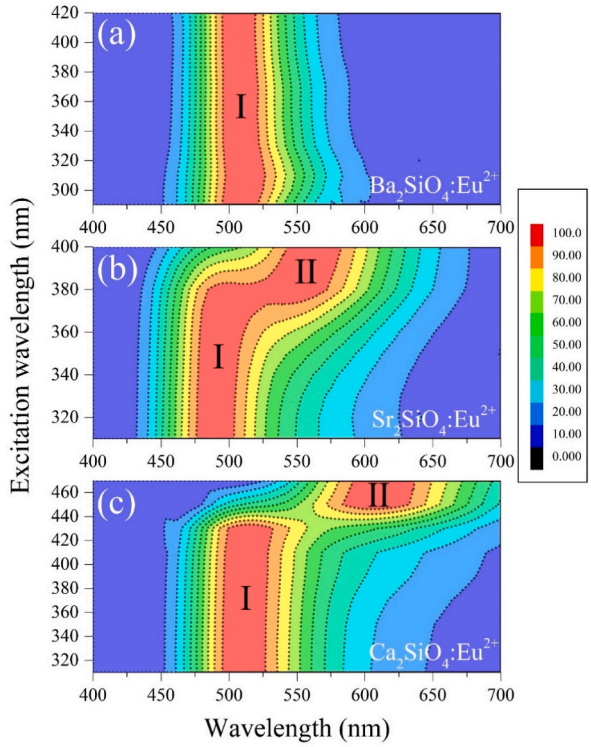

Fig. 7. Contour plot of the PL intensity of (a) $Ba_2SiO_4:Eu^{2+}$, (b) $Sr_2SiO_4:Eu^{2+}$, and (c) $Ca_2SiO_4:Eu^{2+}$ annealed in H_2 atmosphere, measured while varying the photoexcitation wavelength (y-axis).

wavelength increased from 420 to 470 nm (Fig. 7(c)). The strong dependence of the emission wavelength on the substitution doping sites resulted in good tunability of the emission color with excitation wavelength in $Sr_2SiO_4:Eu^{2+}$ and $Ca_2SiO_4:Eu^{2+}$.

3.3.2. Electric potential calculation using point charge model

The positions of peaks I and II are associated with the crystal-field strength of the 5d orbitals of Eu^{2+}. To estimate the strength of the crystal field at the A-site of $A_2SiO_4:Eu^{2+}$, we calculated the electric potential at the A-site caused by the oxygen atoms in the A-O_N complex (N: coordination number) using a simple point-charge model, considering each oxygen ion as a point charge in three-dimensional space. To calculate this, we used the positions of the oxygen ions around the A-site ions obtained from Rietveld refinement. The electric potential V originating from the oxygen complex was estimated using the following equation:

$$V(r) = \sum_{i=1}^{N} \frac{1}{4\pi\varepsilon_0} \frac{q_i}{|r - r_i|} \quad (1)$$

in the calculation, the variables N, ε_0, q_i, and r_i represent the coordinate number of the oxygen complex, the dielectric permittivity in vacuum, the charge of oxygen, and the position of the ith oxygen, respectively. The calculated V values at the A(I) and A(II)sites of A_2SiO_4:Eu are summarized in Table 3. The comparison of the V value according to the A ion used the average of the V values of the α′-phase and β-phases of Sr_2SiO_4.

Remarkably, the V of A_2SiO_4 was in good agreement with the results obtained from the PL spectra. Specifically, as we mentioned above, the positions of Peak I were determined to be 2.48, 2.53, and 2.43 eV for A = Ba, Sr, and Ca, respectively. Correspondingly, the calculated V values at the A(I) site were found to be -87.227×10^{-10}, -89.551×10^{-10}, and -79.840×10^{-10} V for A = Ba, Sr, and Ca, respectively. Similarly, the results obtained for Peak II were consistent with the observations from the PL spectra. As mentioned earlier, the positions of Peak II were determined to be 2.31, 2.30, and 2.18 eV for A = Ba, Sr, and Ca, respectively. The calculated values of V at the A(II) site were found to be -83.105×10^{-10}, -82.983×10^{-10}, and -62.293×10^{-10} V for A = Ba, Sr, and Ca, respectively. Furthermore, the differences in V (ΔV) between Peaks I and II of A_2SiO_4 were $4.122 \bullet 10^{-10}$, $6.567 \bullet 10^{-10}$, and $17.548 \bullet 10^{-10}$ V for A = Ba, Sr, and Ca, respectively. The differences are in good agreement with the PL spectra; the largest ΔV value in Ca_2SiO_4:Eu is consistent with the largest separation between Peak I and Peak II.

3.3.3. Luminescent properties of $A_2SiO_4:Eu^{3+}$

To investigate the emission properties of Eu^{3+} in A_2SiO_4, we examined the emisison spectra of the O_2 annealed samples at $\lambda_{ex} = 395$ nm ($^3F_0$-$^5L_6$ transition of Eu^{3+}). The emission spectra were in good agreement with those reported in previous studies [6,13,36]. As shown in Fig. 8(a–c), the emission peaks of all three samples were commonly observed at approximately 575, 590, 613, 650, and 700 nm, corresponding to the transitions from $^5D_0$ to $^7F_0$, $^7F_1$, $^7F_2$, $^7F_3$, and $^7F_4$ in Eu^{3+} ions, respectively. The common emission pattern in the three $A_2SiO_4:Eu^{3+}$ complexes is in good agreement with the general idea that the transitions between the 4f orbitals are insensitive to the crystal field owing to the screening effect of the 5s and 5p orbitals. For a similar reason, the emission spectra do not clearly reflect the two-site occupation of Eu^{3+} in A_2SiO_4, unlike the emission properties of Eu^{2+} in the H_2 annealed samples. The emission intensity of Eu^{3+} was the highest for $Ca_2SiO_4:Eu^{3+}$, which is in good agreement with the lowest lattice symmetry of $Ca_2SiO_4:Eu^{3+}$ among our samples.

PLE measurements were performed on $A_2SiO_4:Eu^{3+}$. The emission at 700 nm, corresponding to the $^5D_0$-$^7F_4$ transition in Eu^{3+}, was monitored for this measurement. The PLE spectra revealed a broad absorption band in the range of 200–300 nm, which corresponds to the charge transfer (CT) transition from the 2p orbital of the oxygen ion to the 4f orbital of the Eu^{3+} ion. Additionally, sharp peaks were observed at 319, 362, 383, and 395 nm, corresponding to the $^7F_0$-^5H_J, $^7F_0$-$^5D_4$, $^7F_0$-^5G_J, $^5L_7$, and $^7F_0$-$^5L_6$ transition of Eu^{3+}, respectively.

3.3.4. Contrast in luminescent features between Eu^{2+} and Eu^{3+}

Few studies have compared the emission spectra of Eu^{2+} and Eu^{3+} ions in a single-host material [37,38]. In this study, we successfully obtained the luminescent spectra of Eu^{2+} (H_2 annealing) and Eu^{3+} (O_2 annealing) from our samples by simple ambient annealing. Trivalent Eu^{3+} with no electrons in the 5d and 6s orbitals typically exhibits transitions between energy levels of 4f orbitals [39]. It is noted that the parity forbiddent transition between f-orbitals could be forcedly allowed in the non-centrosymmetric structure around Eu^{3+}, without significant disturbance of the crystal field due to the shielding effect on the 5s and 5p outer electrons. For these

Table 3
The calculated electric potential (V) of A_2SiO_4:Eu using the point charge model.

Sample	A-Site	Coordinate	$V_{(0,0,0)}$ (10^{-10} V)	$\Delta V_{(0,0,0)}$ (10^{-10} V)
Ba_2SiO_4:Eu	Ba(I)	10	−87.227	4.122
	Ba(II)	9	−83.105	
α'-Sr_2SiO_4:Eu	Sr(I)	10	−91.887	5.722
	Sr(II)	9	−86.165	
β-Sr_2SiO_4:Eu	Sr(I)	10	−87.215	7.413
	Sr(II)	9	−79.802	
Ca_2SiO_4:Eu	Ca(I)	8	−79.840	17.548
	Ca(II)	7	−62.293	

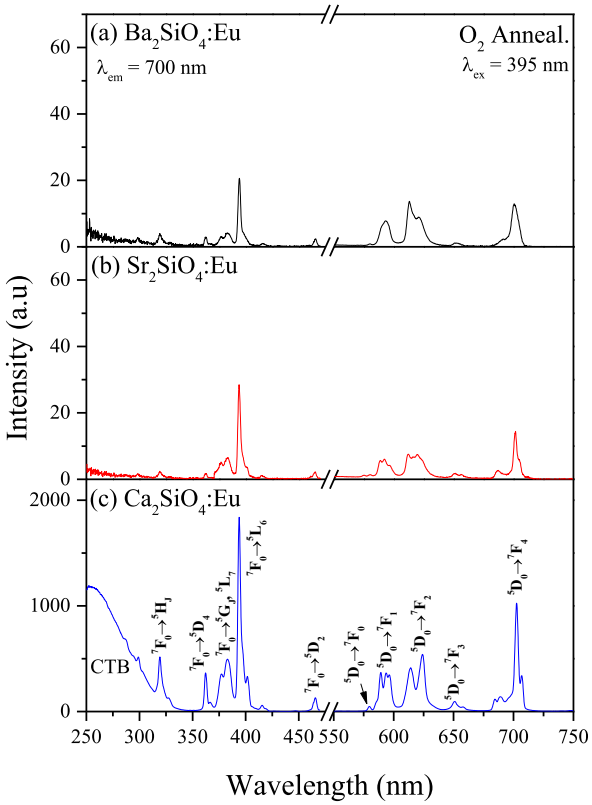

Fig. 8. The PL and PLE spectra of (a) $Ba_2SiO_4:Eu^{3+}$, (b) $Sr_2SiO_4:Eu^{3+}$, and (c) $Ca_2SiO_4:Eu^{3+}$ annealed in an O_2 atmosphere.

reasons, despite the difference in the crystal structure of A_2SiO_4 with respect to the A ion (orthorhombic for A = Ba, a mixture of orthorhombic and monoclinic for A = Sr, and monoclinic for A = Ca), the emission spectral patterns of our samples at approximately 600 nm were quite similar, as shown in Fig. 8. In addition, the f-f transitions in Eu^{3+}, that is, forced electric dipole transitions, should be sensitive to the lattice distortion of the host material. Indeed, the emission intensity of Eu^{3+} increases as the crystal symmetry of A_2SiO_4 decreases in the order of A = Ba, Sr, and Ca; the intensity is much stronger by an order of 2 in Ca_2SiO_4:Eu than in Ba_2SiO_4:Eu. Moreover, Stark splitting was clearly observed for A = Ca because the number of Stark splittings was larger in the lower lattice symmetry.

On the other hand, Eu^{2+} with one more 4f electron than Eu^{3+} shows a $4f^n$-$4f^{(n-1)}5d$ transition, which can be the origin of absorption and emission bands in strong and broad features. Due to the outer 5d orbitals, the spectra of Eu^{2+} lie in a wide spectra ranges with respect to the host material. In Fig. 6, the emission spectra of A_2SiO_4 with Eu^{2+} depend strongly on the A ion (equivalently, the lattice structure of A_2SiO_4) as well as the occupation sites. The emission of Eu^{2+} for A = Ca increased from 500 to 650 nm, whereas the emission for A = Ba was confined to approximately 500 nm. In contrast, the emission intensity of Eu^{2+} appears to be insensitive to the lattice symmetry compared to the emission of Eu^{3+}. The enhancement factor from A = Ca to A = Ba in the Eu^{2+} emission was approximately 2–3, whereas that in the Eu^{3+} emission was approximately 100. Because the 5d-4f transition is parity allowed, symmetry lowering is not essential for the emission of Eu^{2+}.

The TRPL spectra of A_2SiO_4:Eu were obtained to compare the emission decay characteristics of Eu^{2+} and Eu^{3+} (Fig. 9). The PL lifetimes (τ) were calculated using least square fitting with a single (Eu^{3+})/double (Eu^{2+}) exponential functional form. The intensity-weighted average PL lifetime (τ_{avg}) is defined as [40,41].

$$\tau_{avg} = \frac{\sum_i A_i \tau_i^2}{\sum_i A_i \tau_i} \tag{2}$$

where A_i is the amplitude of the ith component and τ_i is the lifetime of the ith component. The decay curves of $A_2SiO_4:Eu^{2+}$ were measured at $\lambda_{em} = 500$ nm upon excitation at $\lambda_{ex} = 395$ nm. As shown in Fig. 9(a), the average PL lifetimes were found to be 4.03–7.33 μs, which are reasonable for the values of the 5d-4f transitions of Eu^{2+} [42]. The decay curves of $A_2SiO_4:Eu^{3+}$ at $\lambda_{em} = 700$ nm were measured at $\lambda_{ex} = 395$ nm excitation. As shown in Fig. 9(b), the average decay times were found to be 1.47–2.51 ms, which are reasonable for the values of the $^5D_0$-$^7F_4$ transitions of Eu^{3+} [43,44]. The decay times of Eu^{2+} are much shorter than those of Eu^{3+}. The obtained parameters of A_2SiO_4:Eu from the TRPL curves are summarized in Table 4.

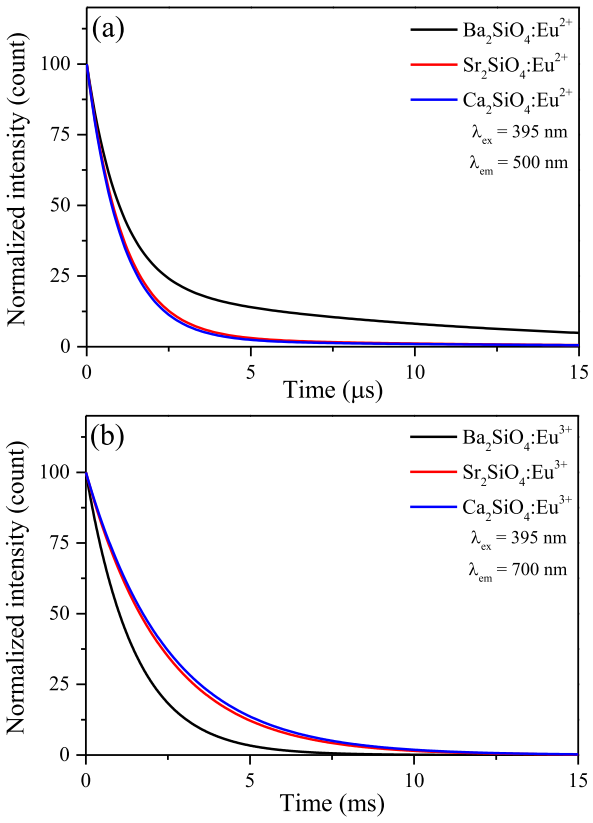

Fig. 9. Measured TRPL decay curves of (a) $A_2SiO_4:Eu^{2+}$ and (b) $A_2SiO_4:Eu^{3+}$ annealed in an H_2/O_2 atmosphere.

Table 4
PL lifetime obtained from fitted TRPL decay and average lifetime of the A_2SiO_4:Eu.

Sample	Anneal	Relative amplitude		PL lifetime		
		A_1	A_2	τ_1	τ_2	τ_{avg}
Ba_2SiO_4:Eu	H_2	0.783	0.217	0.93 μs	9.59 μs	7.33 μs
	O_2	1		1.47 ms		1.47 ms
Sr_2SiO_4:Eu	H_2	0.968	0.032	1.13 μs	12.18 μs	4.03 μs
	O_2	1		2.37 ms		2.37 ms
Ca_2SiO_4:Eu	H_2	0.964	0.036	1.02 μs	11.73 μs	4.21 μs
	O_2	1		2.51 ms		2.51 ms

3.4. CIE coordinates of A_2SiO_4:Eu

The CIE chromaticity coordinates (x, y) calculated from the PL spectra of A_2SiO_4:Eu are shown in Fig. 10 [45]. The CIE coordinates of A_2SiO_4 with Eu^{2+} are marked with solid squares, whereas those of the O_2 annealed A_2SiO_4:Eu (trivalent) are marked with open squares. Interestingly, the CIE coordinates of the H_2 annealed A_2SiO_4:Eu (divalent) varied depending on the excitation wavelength. $Sr_2SiO_4:Eu^{2+}$ and $Ca_2SiO_4:Eu^{2+}$ exhibited turquoise-to-yellow and green-to-red color changes, respectively, depending on the excitation wavelength, whereas $Ba_2SiO_4:Eu^{2+}$ emitted fixed green colors. In contrast, irrespective of the excitation wavelength, the O_2 annealed A_2SiO_4:Eu (trivalent) exhibited red colors: (0.435, 0.325) for A = Ba, (0.621, 0.379) for A = Sr, and (0.63, 0.352) for A = Ca. These results indicate that the emission color of A_2SiO_4:Eu could be fine-tuned over a spectral range from turquoise to red through controling the valence states of Eu ions and the photo-excitation energy.

4. Conclusion

We report on the structures of A_2SiO_4 with doping of Eu ion (A_2SiO_4:Eu), where A = Ba, Sr, or Ca, and their emission properties. Through Rietveld refinement analysis of the XRD measurement data, we found that the structure of Ba_2SiO_4:Eu was orthorhombic, Sr_2SiO_4:Eu existed in a mixed phase of orthorhombic (α′-phase) and monoclinic (β-phase), whereas Ca_2SiO_4:Eu was defect-induced

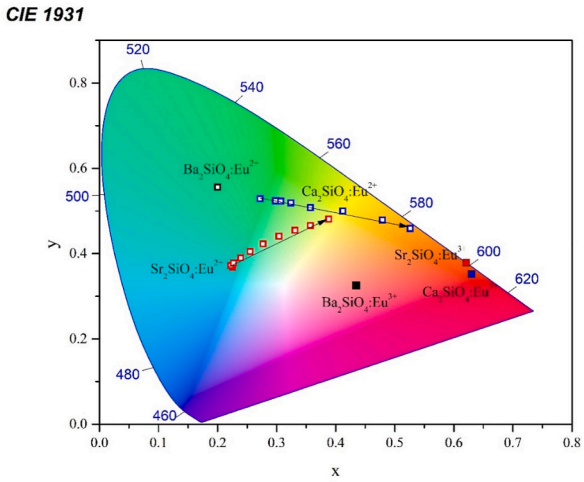

Fig. 10. The CIE coordinates of A_2SiO_4:Eu. The color coordinates of $Sr_2SiO_4:Eu^{2+}$ and $Ca_2SiO_4:Eu^{2+}$ that vary depending on the excitation wavelength are indicated by black arrows.

monoclinic (β-phase). After synthesis, A_2SiO_4:Eu showed typical Eu^{3+} emissions near 600 and 700 nm. With H_2 ambient annealing, a blue-green Eu^{2+} emission emerged near 500 nm, with suppression of the Eu^{3+} emission. The emission of Eu^{2+} depended strongly on the excitation wavelength owing to the two-site occupation of Eu ions, which was most clearly observed in Ca_2SiO_4:Eu. The O_2 annealing restored the Eu^{3+} emission. Conversion between the divalent and trivalent states can be repeated through H_2 and O_2 alternative annealing. Our results show that A_2SiO_4:Eu is a suitable material for comparing the emissions of two Eu ions in a single material and has the potential for use in turquoise-to-red-emitting phosphors for various lighting applications with good tunable color via simple ambient thermal annealing.

Author contribution statement

M. J. Jeong: Conceived and designed the experiments; Performed the experiments; Analyzed and interpreted the data; Wrote the paper.

S. W. Lee: Performed the experiments.

S. W. Wi: Analyzed and interpreted the data; Contributed reagents, materials, analysis tools or data.

K. C. Lee: Analyzed and interpreted the data.

Y. S. Lee: Wrote the paper; Analyzed and interpreted the data.

Data availability statement

Data will be made available on request.

Declaration of competing interest

The authors declare that they have no known competing financial interests or personal relationships that could have appeared to influence the work reported in this paper.

Acknowledgements

This research was supported by the Basic Science Research Program through the National Research Foundation of Korea (NRF), funded by the Ministry of Education (NRF–2021R1A6A1A10044154).

References

[1] Y. Wang, G. Shen, T. Tang, J. Zeng, R.U.R. Sagar, X. Qi, T. Liang, Electrochim. Acta 412 (2022), 140099.
[2] A. Kumawat, K.P. Misra, S. Chattopadhyay, Mater. Technol. 37 (2022) 1595–1610.
[3] E. Radha, D. Komaraiah, R. Sayanna, J. Sivakumar, J. Lumin. 244 (2022), 118727.
[4] J. Wu, L. Zhao, W. Chen, Y. Yang, Y. Wang, X. Xu, Inorg. Chem. Front. 10 (2023) 2474–2483.
[5] S. Qiao, Y. Wang, L. Yin, L. Pan, M. Zhang, P. Townsend, J. Lumin. 243 (2022), 118667.
[6] A. Baran, J. Barzowska, M. Grinberg, S. Mahlik, K. Szczodrowski, Y. Zorenko, Opt. Mater. 35 (2013) 2107–2114.
[7] S. Jang, S. Wi, H. Lim, J.-S. Chung, S. Bu, H. Noh, Y. Lee, J. Alloys Compd. 860 (2021), 157910.
[8] C. Wang, Q. Lv, J. Ma, Y. Li, B. Shao, X. Zhao, G. Zhu, Adv. Powder Technol. 33 (2022), 103394.

[9] I. Nettleship, J.L. Shull Jr., W.M. Kriven, J. Eur. Ceram. Soc. 11 (1993) 291–298.
[10] Y. Luo, D. Jo, K. Senthil, S. Tezuka, M. Kakihana, K. Toda, T. Masaki, D. Yoon, J. Solid State Chem. 189 (2012) 68–74.
[11] C. Guo, Y. Xu, F. Lv, X. Ding, J. Alloys Compd. 497 (2010) L21–L24.
[12] Z. Wang, S. Guo, Q. Li, X. Zhang, T. Li, P. Li, Z. Yang, Q. Guo, Phys. B Condens. Matter 411 (2013) 110–113.
[13] Q. Yanmin, X. Zhang, Y. Xiao, C. Yan, G. Hai, J. Rare Earths 27 (2009) 323–326.
[14] M. Catti, G. Gazzoni, Acta Crystallogr. Sect. B Struct. Sci. 39 (1983) 679–684.
[15] M. Catti, G. Gazzoni, G. Ivaldi, Acta Crystallogr. Sect. C Cryst. Struct. Commun. 39 (1983) 29–34.
[16] K. Yamazaki, H. Nakabayashi, Y. Kotera, A. Ueno, J. Electrochem. Soc. 133 (1986) 657.
[17] Y. Quanmao, L. Yufeng, W. Shan, L. Xingdong, X. Huang, L. Xiaoxia, J. Rare Earths 26 (2008) 783–786.
[18] W. Zhi-Jun, Y. Zhi-Ping, G. Qing-Lin, L. Pan-Lai, F. Guang-Sheng, Chin. Phys. B 18 (2009) 2068.
[19] Y. Sato, H. Kuwahara, H. Kato, M. Kobayashi, T. Masaki, M. Kakihana, Opt Photon. J. 5 (2015) 326.
[20] S. Poort, W. Janssen, G. Blasse, J. Alloys Compd. 260 (1997) 93–97.
[21] L.-C. Ju, C. Cai, Q.-Q. Zhu, J.-Y. Tang, L.-Y. Hao, X. Xu, J. Mater. Sci. Mater. Electron. 24 (2013) 4516–4521.
[22] L.-C. Ju, X. Xu, L.-Y. Hao, Y. Lin, M.-H. Lee, J. Mater. Chem. C 3 (2015) 1567–1575.
[23] S.-Y. Zheng, J.-W. Chiou, Y.-H. Li, C.-F. Yang, S.C. Ray, K.-H. Chen, C.-Y. Chang, A.R. Shelke, H.-T. Wang, P.-H. Yeh, Sci. Rep. 10 (2020), 12725.
[24] M.G. Ha, J.-S. Jeong, K.-R. Han, Y. Kim, H.-S. Yang, E.D. Jeong, K. Hong, Ceram. Int. 38 (2012) 5521–5526.
[25] X. Lu, S. Wang, S. Liu, P. Du, Z. Ye, X. Geng, X. Cheng, J. Phys. Chem. C 123 (2019) 13877–13884.
[26] J. Wen, Y.-Y. Yeung, L. Ning, C.-K. Duan, Y. Huang, J. Zhang, M. Yin, J. Lumin. 178 (2016) 121–127.
[27] Y.M. Kim, S.H. Hong, J. Am. Ceram. Soc. 87 (2004) 900–905.
[28] Z. Hao, J. Zhang, X. Zhang, Y. Luo, L. Zhang, H. Zhao, J. Lumin. 152 (2014) 40–43.
[29] I. Gupta, S. Singh, P. Kumar, S. Bhagwan, V. Kumar, D. Singh, Curr. Appl. Phys. 43 (2022) 78–89.
[30] R. Cao, X. Wang, X. Ouyang, Y. Jiao, Y. Li, H. Wan, W. Li, Z. Luo, J. Lumin. 224 (2020), 117292.
[31] S. Xiaoyuan, J. Zhang, X. Zhang, L. Yongshi, W. Xiaojun, J. Rare Earths 26 (2008) 421–424.
[32] J. Sun, H. Lin, D. Zhang, R. Hong, C. Tao, Z. Han, Ceram. Int. 45 (2019) 23643–23650.
[33] M. Grinberg, J. Barzowska, A. Baran, B. Kukliński, Materials Science-Poland 29 (2011) 272–277.
[34] K. Asami, J. Ueda, K. Yasuda, K. Hongo, R. Maezono, M.G. Brik, S. Tanabe, Opt. Mater. 84 (2018) 436–441.
[35] S.S.B. Nasir, K. Yakura, N. Horiuchi, M. Tsuta, A. Kato, J. Phys. Chem. Solid. 133 (2019) 135–141.
[36] D.H. Kim, J.H. Kim, J. Kor. Phys. Soc. 80 (2022) 257–264.
[37] M.-F. Volhard, T. Jüstel, Opt Commun. 410 (2018) 617–622.
[38] D. Lee, M. Kwark, D. Kim, S. Wi, J.-S. Chung, I.W. Kim, Y.-J. Kwark, Y. Lee, J. Kor. Phys. Soc. 81 (2022) 646–652.
[39] D. Lee, I. Chan, M. Jeong, Y. Lee, Curr. Appl. Phys. 46 (2023) 14–20.
[40] J. Solé, L. Bausa, D. Jaque, An Introduction to the Optical Spectroscopy of Inorganic Solids, John Wiley & Sons, 2005.
[41] A. Pradhan, P. Pal, G. Durocher, L. Villeneuve, A. Balassy, F. Babai, L. Gaboury, L. Blanchard, J. Photochem. Photobiol. B Biol. 31 (1995) 101–112.
[42] A. Sillen, Y. Engelborghs, Photochem. Photobiol. 67 (1998) 475–486.
[43] S. Poort, A. Meyerink, G. Blasse, J. Phys. Chem. Solid. 58 (1997) 1451–1456.
[44] S.K. Gupta, M. Mohapatra, S. Kaity, V. Natarajan, S. Godbole, J. Lumin. 132 (2012) 1329–1338.
[45] I. Gupta, S. Singh, P. Kumar, S. Bhagwan, V. Kumar, D. Singh, Curr. Appl. Phys. 43 (2022) 78–89.